Journal of Sol-Gel Science and Technology (2023) 105:220–236
https://doi.org/10.1007/s10971-022-05981-z

ORIGINAL PAPER: SOL-GEL AND HYBRID MATERIALS FOR CATALYTIC, PHOTOELECTROCHEMICAL, AND SENSOR APPLICATIONS

Photoreduction of Cr(VI) on $B_4C/AgFe_2O_4$ composite

Ozcan Koysuren[1] · Hafize Nagehan Koysuren[2]

Received: 6 August 2022 / Accepted: 24 October 2022 / Published online: 5 November 2022

Abstract

The present study aimed to couple boron carbide (B_4C) and silver ferrite ($AgFe_2O_4$) in the composite structure for the Cr(VI) photoreduction application. B_4C was synthesized through a heat treatment process of a polymer precursor, polyvinyl borate (PVB). $B_4C/AgFe_2O_4$ composites were obtained by the synthesis of $AgFe_2O_4$ using a auto-combustion technique in the presence of the as-prepared B_4C. Fourier-transform infrared spectroscopy and X-ray powder diffraction analyses revealed that pure B_4C, pure $AgFe_2O_4$, and the $B_4C/AgFe_2O_4$ composites were synthesized successfully. Field emission scanning electron microscopy and N_2 adsorption-desorption studies exhibited that the as-prepared samples had similar surface morphology. The $B_4C/AgFe_2O_4$ composites can absorb a significant part of the visible light and can be used as visible-light-driven photocatalyst, shown by UV-Vis absorption spectroscopy. Coupling B_4C with $AgFe_2O_4$ in the composite structure provided enhancement in the Cr(VI) photoreduction efficiency. The Cr(VI) removal rate of pure B_4C increased from 65.1% to 98.0% within 120 min. of visible light irradiation. The resulting enhancement in the Cr(VI) photoreduction efficiency was attributed to the suppression of the recombination of the photoexcited charge carriers on the composites, which was shown by photoluminescence spectroscopy. Under acidic conditions, the Cr(VI) removal rate in the presence of $B_4C/AgFe_2O_4$ increased to almost 99%. The Cr(VI) photoreduction efficiency decreased to 89.9% when real wastewater spiked with Cr(VI) ions was used instead of the simulated Cr(VI) solution. It was observed that the prepared composites were reusable for the Cr(VI) removal process and magnetically separable from the Cr(VI) solution.

Graphical abstract

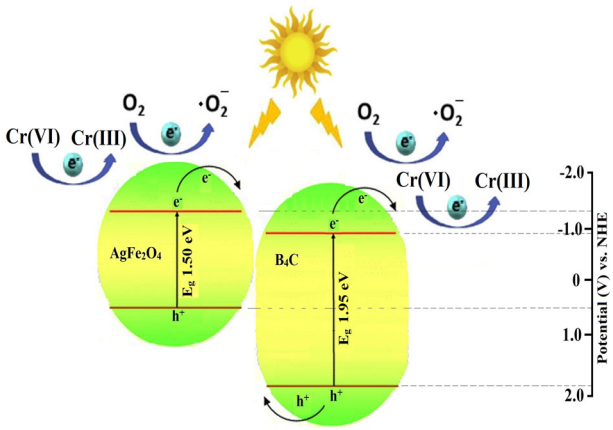

Supplementary information The online version contains supplementary material available at https://doi.org/10.1007/s10971-022-05981-z.

✉ Ozcan Koysuren
koysuren@ankara.edu.tr

[1] Department of Energy Engineering, Ankara University, Ankara 06830, Turkey

[2] Department of Environmental Engineering, Kirsehir Ahi Evran University, Kirsehir 40100, Turkey

Keywords B_4C · $AgFe_2O_4$ · Cr(VI) photoreduction · Photocatalytic activity

Highlights

- Highly toxic Cr(VI) was converted to less toxic Cr(III) through the photoreduction process.
- Coupling B_4C with $AgFe_2O_4$ promoted the separation of the photogenerated charge carriers of the composite constituents, providing enhancement in the CrVI photoreduction efficiency.
- Within 120 min., almost all of the Cr(VI) was removed from the aqueous solution.
- Reusable and magnetically separable composites were synthesized.

1 Introduction

Cr(VI) is known as one of the heavy metal ions found in wastewater [1]. It is released into environment through the wastewater of various industries such as metal plating, oil refining, power generation, leather manufacturing, and textile. Cr(VI) ion is highly mobile and also toxic. Cr(VI) ion, illustrating carcinogenic and mutagenic tendencies, is considered as a high-priority pollutant. Cr(VI) is known as a toxic ion because it easily penetrates the living cell and causes poisoning of the living cell [2]. Different techniques, including microbial reduction [3], adsorption [4], chemical precipitation [5], and membrane filtration [6], have been applied to remove Cr(VI) ion from the wastewater. The mentioned techniques include many disadvantages such as large amount of chemical consumption, chemical sludge formation as a by-product, and high treatment cost [7]. On the other hand, Cr(III) is another stable oxidation state of chromium. Unlike Cr(VI), Cr(III) is less toxic and it is regarded safe in drinking water. The reduction of Cr(VI) to Cr(III) is important for the living beings and the environment [2]. As an alternative to the mentioned techniques, photocatalytic reduction has been found to be an efficient and environmentally promising option as toxic Cr(VI) can be easily reduced to less toxic Cr(III) [1, 8]. The photoreduction technique is highly economical and sustainable. It requires simple and minimal processes and this technique is devoid of sludge formation [2].

Various semiconductors, including TiO_2 [9], ZrO_2 [10], CuO [11], ZnO [12], and g-C_3N_4 [13], have been investigated as a potential photocatalyst to remove Cr(VI) from the wastewater through the photoreduction process. However, most of the photocatalysts, such as TiO_2 and ZnO, illustrate limited photoreduction performance owing to their poor Cr(VI) adsorption ability. Due to their wide optical band gap, they can adsorb a narrow part of the visible light [1]. In addition, undesired photogenerated electron-hole recombination is inevitable to the mentioned photocatalysts. Therefore, for the photoreduction of Cr(VI) to Cr(III), it is important to obtain highly efficient photocatalysts with a low recombination rate of the photoexcited charge carriers and a wide visible light absorption range [8]. Recently, B_4C, which is a metal-free photocatalyst driven by visible light, has attracted considerable interests. The light absorption ability of B_4C covers almost the entire visible spectrum. The stability and abundance of B_4C are seen as significant advantages over conventional metal oxide photocatalysts [14]. B_4C can be synthesized in powder form by carbothermal reduction reaction of boric acid or boron oxide at high temperatures (1500–2000 °C) or by magnesiothermal reaction of boron oxide with Mg metal between 1000–1800 °C [15, 16]. In addition, plasma-assisted chemical vapor deposition method [17], molten salt-assisted combustion technique [18], pulsed electric current sintering technique [19], and sol-gel method [20] have been applied to synthesize B_4C in powder form. However, the mentioned methods have several disadvantages such as expensive raw materials, high reaction temperatures ($T > 1000$), complex equipment and long reaction times [14, 18]. Apart from the methods mentioned, B_4C can be synthesized in powder form using a polymer precursor through exothermic reactions at relatively low temperatures [15, 17, 21]. In this context, polyvinyl borate (PVB), precursor polymer, can be synthesized using non-toxic and low-cost chemicals, and then PVB has the potential to be converted into B_4C nanoparticles by a heat treatment. The synthesis of B_4C nanoparticles by a heat treatment of the precursor polymer also provides the advantages of low energy consumption and high product purity [15, 17]. It is quite important to reduce the heat treatment temperature and to increase the crystal purity of B_4C for its potential applications like solar energy conversion. In literature, Yan et al. (2019) succeeded in reducing the heat treatment temperature to 850 °C using Fe, Ni, Co, Zn, and Cu catalysts to prepare B_4C nanoparticles from elemental boron and carbon [14]. On the other hand, da Rocha and de Melo (2011) added B_4C seed crystals to the reaction medium to convert boric acid and graphite into B_4C nanoparticles through the heat treatment process. They provided complete conversion of the reactants to B_4C in the presence of 2.5 wt.% B_4C seed crystals at 1750 °C [22].

Due to the crystal defects and distortions in its structure, B_4C has a narrow optical band gap energy and exhibits strong absorption in the visible light region [23]. In

addition, the unique structure of the three-center two-electron bond and the self-induced distortion of the icosahedron units of B_4C extend the lifetime of the photoexcited charge carriers and lowers the conduction band potential. All these properties demonstrate the potential of B_4C as a photocatalyst under visible light [14, 24]. Although the crystal defects and distortions enhance the visible light absorption ability of B_4C, they can cause to form midgap energy states within the band gap, promoting the recombination of the photoexcited charge carriers [23]. To solve the mentioned problem, the formation of internal electric field in photocatalyst through a heterojunction structure has been known to be an effective strategy to suppress the recombination of the photogenerated charge carriers [24]. To form an effective heterojunction with B_4C, it is important to find a semiconductor with appropriate band potentials. In literature, various semiconductors such as BiOI [25], TiO_2 [26], g-C_3N_4 [24], and ZnO [27] have been preferred as a photocatalyst to couple with B_4C in the heterojunction structure. Silver Ferrite ($AgFe_2O_4$) is a suitable semiconductor for the heterojunction structure in the photocatalytic process owing to its magnetic behavior with a narrow band gap energy [28]. It is easy to synthesize $AgFe_2O_4$ particles. $AgFe_2O_4$ exhibits superior properties such recyclability, reusability, eco-friendly, chemical, and photochemical stability [29]. In addition, Ag as a noble metal has been known to be effective for promoting the separation of the photoexcited charge carriers [30].

Although there are studies in the literature on the use of polycrystalline ferrites such as $ZnFe_2O_4$ [31], $CaFe_2O_4$ [32], $CuFe_2O_4$ [33], $NiFe_2O_4$ [34] and $MgFe_2O_4$ [35] for the removal of Cr(VI) from the wastewater by the photoreduction process (Table 1), there is no study on the removal Cr(VI) using $AgFe_2O_4$ as a photocatalyst. When compared with polycrystalline ferrite photocatalysts (Table 1), very high Cr(VI) removal could not be obtained with the $AgFe_2O_4$ photocatalyst alone. On the other hand, there are very few studies on the photocatalytic activity of $AgFe_2O_4$. Nas (2021) studied the photocatalytic dye degradation efficiency of $AgFe_2O_4$/carbon nanotube composites. He obtained 98.5% dye (methylene blue) degradation efficiency within 75 min [30]. In a different study, Singh et al. (2021) obtained 61.2% dye (methylene blue) degradation efficiency at the end of 60 min. with $AgFe_2O_4$, synthesized through a novel auto-combustion technique [29]. Sanadi and Kamble (2018) synthesized $AgFe_2O_4$ nanoparticles using the auto-combustion technique. The percent degradation of the model dye (Rhodamine-B) was 92% at the end of 150 min [36]. In addition, Mao et al. (2022) prepared $AgFe_2O_4/BiFeO_3$ composites, which provided the dye (methylene blue) degradation of about 99% in 120 min. under visible light irradiation. The photocatalytic activity of $AgFe_2O_4$ in the composite structure was higher than that of pure $AgFe_2O_4$ due to the high recombination rate of the photogenerated charge carriers [28]. Considering the energy band structure, the coupling of B_4C with $AgFe_2O_4$ is expected to suppress the recombination of the photoexcited charge carriers. In the present manuscript, B_4C was prepared through the heat treatment of a polymer precursor, polyvinyl borate, synthesized through the crosslinking reaction of boric acid and polyvinyl alcohol. Then, B_4C and $AgFe_2O_4$ was coupled within the composite structure though the facile synthesis of $AgFe_2O_4$ by the auto-combustion technique in the presence of the as-prepared B_4C. Further, $B_4C/AgFe_2O_4$ composites were experimented as an efficient visible-light-driven photocatalyst for the photoreduction of Cr(VI). This is the first report ever for the photoreduction of Cr(VI) by the $B_4C/AgFe_2O_4$ composite with a high removal rate of 98.0% in 120 min. Compared to pure polycrystalline ferrites and the composites containing polycrystalline ferrites (Table 1), considerably higher Cr(VI) removal was achieved within 120 minutes under visible light irradiation.

Table 1 Comparison with previous reports of polycrystalline ferrite nanoparticles

Photocatalyst	Light source	Cr(VI) removal rate
$ZnFe_2O_4/TiO_2$ [31]	Visible light (200 W)	~60% in 150 min.
$CuFe_2O_4/CdS$ [33]	Visible light (200 W)	~60% in 250 min.
$NiFe_2O_4$ [34]	Visible light (105 W)	~26% in 60 min.
$MgFe_2O_4$ [35]	Visible light ($\lambda > 420$ nm)	~84% in 160 min.
$CaFe_2O_4/ZnO$ [32]	Natural sunlight	~42% in 240 min.

2 Experimental

2.1 Materials and methods

B_4C particles were synthesized through the heat treatment of a polymer precursor, polyvinyl borate, which was synthesized through the crosslinking reaction between polyvinyl alcohol (PVA) and boric acid (H_3BO_3) in a PVA/H_3BO_3 molar ratio 4.2/1 [15]. 2.47 g of PVA was dissolved in 50 ml of distilled water at 80 °C. In order to increase the B_4C crystal purity of the final product, B_4C seed crystals (5 wt%, 40-60 nm in size) were added into the PVA solution [22]. In addition, Ni (Nickel nitrate hexahydrate) catalyst (2.5 wt.%) was added into the PVA solution to improve the crystallinity of the final product during the heat treatment process [14]. On the other side, 0.795 g of boric acid was dissolved in 50 ml of distilled water at room temperature using a magnetic stirrer. Then, the as-prepared boric acid solution was added into the PVA solution. The resulting solution was kept under stirring at 80 °C for half an hour. The resulting PVB gel was separated from its solution and

were dried in an oven at 120 °C for 24 h. The dried PVB gel was ground into fine powders. Afterward, a heat treatment was applied to the PVB powder. For this purpose, they were placed in an alumina crucible and heated at 1000 °C for 3 hours in Ar flow [15]. To separate the final product from Ni catalyst, B_4C was kept under stirring in concentrated HNO_3 solution for 60 min. Then, B_4C particles was filtered and rinsed with distilled water. After drying at 120 °C, B_4C powder was obtained [14].

$B_4C/AgFe_2O_4$ composites were synthesized through a sol-gel auto-combustion technique in the presence of the as-prepared B_4C powder [36]. In detail, 0.170 g (1 mmol) of silver nitrate ($AgNO_3$) and 0.808 g (2 mmol) of iron nitrate ($Fe(NO_3)_3{\cdot}9H_2O$) were dissolved in 10 ml of distilled water, including the as-prepared B_4C powder. To enhance the active surface area of the $AgFe_2O_4$ phase in the composite, 0.05 g of poly(ethylene glycol) (PEG: 200 g/mol) as a template chemical was added into the reaction medium. The PEG template was supposed to convert the $AgFe_2O_4$ surface to mesoporous form [37]. Then, 0.384 g of citric acid ($C_6H_8O_7$) was added into the resulting solution and kept stirring using a magnetic stirrer. The pH of the resulting solution was changed to be 8.0 using HCl and ammonia. Afterward, the as-prepared solution was heated at 100 °C under constant stirring. After all water was evaporated, the solution was converted into a gel. Afterwards, the resulting gel started to burn through a self-propagating combustion reaction and turned into a fine powder [36]. To separate the PEG template from the $AgFe_2O_4$ phase of the composite, the resulting powder was rinsed with distilled water and dried at 100 °C for 24 hours. Finally, the powder was exposed to a heat treatment at 800 °C for 60 min. and $B_4C/AgFe_2O_4$ composite in powder form was obtained [29]. Pure $AgFe_2O_4$ and the composite with different weight ratio of $B_4C/AgFe_2O_4$ (10/1, 10/2, 10/3, 10/4 and 10/5) were synthesized following the same procedure. The composite samples were labed as $B_4C/AgFe_2O_4$(10/1), $B_4C/AgFe_2O_4$(10/2), $B_4C/AgFe_2O_4$(10/3), $B_4C/AgFe_2O_4$(10/4) and $B_4C/AgFe_2O_4$(10/5), respectively, depending on the weight ratio of B_4C to $AgFe_2O_4$.

2.2 Structural, morphological and optical characterization

Fourier-transform infrared (FTIR) spectroscopy of pure B_4C, pure $AgFe_2O_4$, and the composite samples was obtained using Bruker IFS 66/S model spectrophotometer. X-ray diffraction (XRD) pattern of the as-prepared samples was acquired using Rigaku Ultima IV model X-ray diffractometer with monochromated CuKα radiation. The morphology of pure B_4C, pure $AgFe_2O_4$ and the composite samples was investigated using a field emission scanning electron microscope (FESEM, QUANTA 400F). The elemental composition of the composite sample was investigated by energy dispersive X-ray (EDX) spectroscopy (JXA-8230 EDX Microanalysis Instrument). The specific surface area and pore size distribution of the as-prepared samples were investigated through N_2 adsorption-desorption studies (Quantachrome Corporation, Autosorb-6) using Brunner-Emmett-Teller (BET) and Barret-Joyner-Halender (BJH) methods. The point of zero charge (PZC) value of $B_4C/AgFe_2O_4$ composite was determined using the electrophoretic mobility method (MALVERN Nano ZS90) with zeta potential measurement. The UV-Vis absorption spectroscopy of the prepared samples was obtained within a wavelength range of 200–800 nm using a UV-Vis spectrophotometer (Genesys 10S, Thermo Scientific). The photoluminescence spectrum of the prepared samples was recorded at room temperature on Jobin Yvon Florong-550 Lumina model spectrophotometer at the excitation wavelength of 325 nm. The saturation magnetization value of $AgFe_2O_4$ and the $B_4C/AgFe_2O_4$ composites were measured with a vibrating sample magnetometer (VSM, Cryogenic Limited PPMS) under magnetic field at room temperature.

2.3 Characterization of the Cr(VI) photoreduction performance

The Cr(VI) photoreduction experiment was carried out under visible light irradiation, provided by a 300 W (Osram Ultravitalux) lamp. The simulated Cr(VI) solution (20 mg/l) was prepared by dispersing 2 mg of $K_2Cr_2O_7$ in 100 ml of distilled water. The photocatalyst sample (50 mg) was dispersed in the Cr(VI) solution. Then, the solution was kept in dark for half an hour to attain adsorption-desorption equilibrium. Afterward, Cr(VI) solution was exposed to visible light irradiation. The photoreduction unit was ventilated by a fan to prevent the temperature of the Cr(VI) solution from rising. During the visible light irradiation, 2 ml of sample was extracted from the solution every 20 min. Afterward, the solution sample was centrifuged to separate the photocatalyst particles from the extracted Cr(VI) solution. Then, diphenylcarbazide (DPC) photometric technique was applied to the supernatant solution to determine its Cr(VI) composition. In detail of the DPC technique, 2 ml of the centrifuged Cr(VI) solution was mixed with 1 ml of sulphuric acid (0.2 M) and 1 ml of 1,5-diphenylcarbazide (0.5% w/v). After 5 min., the absorbance of the resulting solution (Cr(VI)-diphenylcarbazide complex) was measured at 543 nm using the UV-Vis spectrophotometer [38]. The Cr(VI) photoreduction rate was calculated using the following Eq. (1):

$$\text{Cr(VI) photoreduction rate}\,(\%) = (C_0 - C) \times 100/C_0 \quad (1)$$

where C_0 and C indicated the initial Cr(VI) concentration and the residual Cr(VI) concentration after the photoreduction reaction [39].

To investigate the Cr(VI) photoreduction mechanism, potassium persulfate (1 mM) an electron scavenger and ammonium oxalate (1 mM) as a hole scavenger were added into the simulated Cr(VI) solution [40–42]. To investigate the effect of the initial solution pH on the Cr(VI) photoreduction efficiency, the pH of the simulated Cr(VI) solution was changed between 2 and 10 using 1 mol/l HCl and 1 mol/l NaOH [43]. In order to evaluate the effect of the initial solution concentration on the Cr(VI) removal rate, the simulated Cr(VI) solution with different initial solutions concentrations of Cr (VI) (10, 15, 20, 25, and 30 mg/l) was prepared [44]. In addition, the $B_4C/AgFe_2O_4$(10/4) concentration was changed in the range of 0.1–1.0 g/l to examine the effect of photocatalyst concentration in the simulated Cr(VI) solution. To study the ability of the photocatalyst to be reused multiple times, the $B_4C/AgFe_2O_4$ composite was recovered from the simulated Cr(VI) solution using magnetic separation. Then, the composite sample was kept under stirring in H_2O_2 (30%) solution for half an hour. After rinsing with distilled water and drying at 80 °C, the composite particles were used for the following Cr(VI) photoreduction cycle [45]. In order to understand the effect of the water matrix on the photoreduction efficiency of Cr(VI), ammonium chloride (1 g/l) and sodium sulfate (0.4 g/l) that are mostly present in the real wastewater environment and/or commonly used in wastewater treatment processes, were added separately to the simulated Cr(VI) solution [45].

3 Results and discussion

3.1 FTIR analysis

Figure 1a exhibits FTIR spectrum of pure B_4C, prepared through the heat treatment of PVB polymer precursor. The characteristic peak at 570 cm^{-1} and 547 cm^{-1} were assigned to the C-B-C bending vibration [46]. The peaks at 644 cm^{-1}, 715 cm^{-1}, 884 cm^{-1} and 1194 cm^{-1} might belong to the B–C stretching vibration [46, 47]. The presence of the peaks belonging to the B-C and C-B-C bonds confirmed the successful conversion of the polymer precursor to B_4C [46]. The narrow band at around 3210 cm^{-1} and the transmittance peak at 1742 cm^{-1} were attributed to the −OH and C = O stretching vibrations, respectively [46, 48]. In addition, the transmittance peaks at around 1379 cm^{-1} and 1449 cm^{-1} were assigned to the B–O stretching vibration [48, 49]. There is an additional transmittance peak at 1231 cm^{-1}, attributed to icosahedral vibrations of B_4C [49]. PVB precursor polymer was synthesized through the crosslinking reaction between PVA and boric acid to form B–O–C bond. During the heat treatment of PVB at around 600 °C, micron-size B_2O_3 particles, dispersed in a carbon matrix, are formed. Then, B_4C particles are formed through the carbothermal reduction of B_2O_3 at higher temperature (T > 1000 °C) (2) [50].

$$2B_2O_3 + 7C \leftrightarrow B_4C + 6CO \quad (2)$$

The peaks belonging to the B–O stretching vibration might arise from the B_2O_3 structure that could not be converted to B_4C through the carbothermal reduction reaction. However, the absence of the characteristic peaks assigned to the C–H and B–O stretching vibrations at 2360 cm^{-1} and 924 cm^{-1}, respectively, indicated a high conversion of the B_2O_3 and carbon phases to B_4C [49].

To determine the successful synthesis of $AgFe_2O_4$, FTIR spectrum of both pure $AgFe_2O_4$ and $AgFe_2O_4$ composites prepared in the presence of B_4C particles were recorded (Fig. 1b–d). The existence of the transmittance peaks corresponding to metal-oxygen bonds in the range of 750–400 cm^{-1} confirmed the successful synthesis of $AgFe_2O_4$ (Fig. 1b) [29]. The appearance of the peak at 516 cm^{-1} might be caused by the stretching vibration of the Fe-O bond [29]. In addition, the sharpness of this peak indicates the degree of crystallinity. The mentioned transmittance peak was the most intense peak of the FTIR spectrum of $AgFe_2O_4$, indicating the success of the $AgFe_2O_4$ synthesis. A weak transmittance peak at 1366 cm^{-1} indicated the presence of some residual nitrate group in the synthesized sample [51]. The presence of the mentioned peak indicated that all of the silver nitrate and iron nitrate were not used during the $AgFe_2O_4$ synthesis. However, the absence of the transmittance peak at 2365 cm^{-1} corresponding to the stretching vibration of the C–H bond indicated that there was no residual citric acid in the prepared sample [51]. The other peak at around 1737 cm^{-1} might be due to the bending vibration of -OH molecule [51]. In addition, the weak transmittance peak observed at 1067 cm^{-1} might be due to the stretching vibration of the octahedral metal-oxygen bond [51].

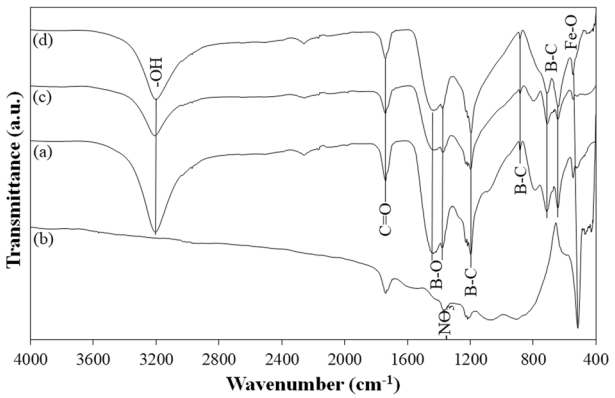

Fig. 1 FTIR spectrum of **a** B_4C, **b** $AgFe_2O_4$, **c** $B_4C/AgFe_2O_4$(10/2) and **d** $B_4C/AgFe_2O_4$(10/4)

FTIR spectrum of the $B_4C/AgFe_2O_4$ composites are revealed in Fig. 1c, d. The peak at 546 cm^{-1} might be originated due to the stretching vibration of the Fe–O bond of $AgFe_2O_4$ and/or the stretching vibration of the C–B–C bond of B_4C [29, 46, 47]. Both peaks appeared to overlap at 546 cm^{-1}. Compared to $B_4C/AgFe_2O_4$(10/2), a significant increase in the mentioned peak intensity on the FTIR spectrum of $B_4C/AgFe_2O_4$(10/4) was observed. The observed increase in the mentioned peak intensity revealed the dominant effect of the Fe-O bond. FTIR spectrum of both composites exhibits the transmittance peaks at 644 cm^{-1}, 711 cm^{-1}, 884 cm^{-1}, 1198 cm^{-1}, which were attributed to the stretching vibration of the B–C bond [46, 47]. The transmittance peaks at 1228 cm^{-1} and 1373 cm^{-1} were attributed to the icosahedral vibrations of B_4C and the stretching vibration of the B–O bond, respectively [49]. In addition, the peak observed at 1449 cm^{-1} in the FTIR spectrum of both composite samples might belong to the stretching vibration of the B–O bond formed on the B_4C surface [48]. Similar to the FTIR spectrum of pure B_4C, there are transmittance peaks at 1739 cm^{-1} and 3208 cm^{-1} belonging to the C=O stretching vibration and -OH stretching vibration, respectively [46–48]. Compared to pure B_4C and pure $AgFe_2O_4$, there are shifts in the wave number of the transmittance peaks observed on the FTIR spectrum of the composites, which might be due to the interaction of the composite constituents within the composite structure.

3.2 XRD analysis

On the XRD diffractogram of pure B_4C (Fig. 2a), there are diffraction peaks at 21.9°, 23.4°, 31.8°, 34.9°, 37.8°, 39.1°, 53.4°, 61.7°, 63.6°, 64.5°, 66.6°, 70.3°, 71.2°, 71.7°, and 75.3°, which might be indexed to (003), (012), (110), (113), (021), (113), (205), (303), (125), (018), (220), (131), (223), (312) ve (306) planes of the rhombedral B_4C crystal structure (JCPDS No. 26-232). In addition, there are a wide diffraction peak between 20°-30° and a small diffraction peak at 27.8°, which were attributed to the amorphous carbon phase and B_2O_3, respectively [50]. The presence of the mentioned diffractioned peaks revealed that all of the B_2O_3 and carbon phases could not be converted to B_4C through the carbotermal reduction reaction [50]. The diffraction peak intensities indicated that the B_4C crystal structure was successfully obtained. The mean crystal size of the B_4C particles was calculated using the Scherrer Eq. (3) [52]:

$$Dp = (0.94\,\lambda)/(\beta\,Cos\theta) \quad (3)$$

where Dp is the mean crystal size of the B_4C particle, λ is the X-ray wavelength, β is full width at half maximum of the main diffraction peak and θ is the Bragg angle. The mean crystal size of pure B_4C was calculated as 28.67 nm. On the XRD diffractogram of pure $AgFe_2O_4$ (Fig. 2b), there are diffraction peaks at 33.2°, 35.6°, 38.1°, 44.4°, 49.5°, 54.1°, 62.4°, 64.4° ve 77.5°, indexed to (220), (310), (311), (321), (411), (421), (313), (520) and (620) planes of the cubic $AgFe_2O_4$ crystal structure [29]. All the diffraction peaks of $AgFe_2O_4$ were seen on the XRD diffractogram (Fig. 2b), indicating that $AgFe_2O_4$ was successfully synthesized. The sharp diffraction peaks also showed that the crystal structure was formed successfully during the heat treatment process. The mean crystal size of $AgFe_2O_4$ was calculated as 56.0 nm.

On the XRD diffractogram of the $B_4C/AgFe_2O_4$(10/2) composite, the diffraction peaks were observed at 22.3°, 23.5°, 31.3°, 32.5°, 34.9°, 38.1°, 44.3°, 64.4° and 77.5° (Fig. 2c). Compared to pure B_4C and pure $AgFe_2O_4$, the characteristic diffraction peaks of the composite constituents were observed slightly at different diffraction angles, indicating possible interaction between B_4C and $AgFe_2O_4$ within the composite matrix. Although the B_4C phase constitutes the majority phase in the composite structure, it was seen that the characteristic diffraction peaks of $AgFe_2O_4$ (38.1°, 44.4°, and 77.5°) were more prominent. On the XRD diffractogram of the $B_4C/AgFe_2O_4$(10/4) composite, the diffraction peaks were detected at 25.4°, 33.3°, 38.1°, 38.9°, 43.4°, 44.3°, 45.02°, 52.1°, 54.9°, 55.6°, 62.7°, 64.4°, 66.9°, 70.5° and 77.4° (Fig. 2d). A significant increase was noticed in the intensity of the diffraction peaks at 25.4° and 33.3°, belonging to B_4C and $AgFe_2O_4$, respectively. It was thought that the main diffraction peaks of both B_4C and $AgFe_2O_4$ at 37.8° and 38.1° might combine (Fig. 2c, d). When the Scherrer equation was applied to the combined peak, the mean crystal size of the $B_4C/AgFe_2O_4$(10/2) and $B_4C/AgFe_2O_4$(10/4) composite samples was calculated as 39.7 nm and 51.8 nm, respectively. Increasing the $AgFe_2O_4$ phase in the composite structure significantly increased the mean crystal size.

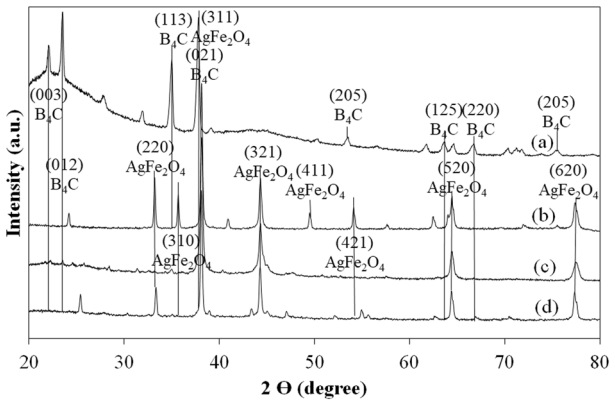

Fig. 2 XRD spectrum of **a** B_4C, **b** $AgFe_2O_4$, **c** $B_4C/AgFe_2O_4$(10/2) and **d** $B_4C/AgFe_2O_4$(10/4)

3.3 Photoluminescence study

To reveal the effect of coupling B_4C with $AgFe_2O_4$ in the composite structure, photoluminescence (PL) spectrum of B_4C, $AgFe_2O_4$, $B_4C/AgFe_2O_4$(10/2), and $B_4C/AgFe_2O_4$(10/4) were compared on Fig. 3. The main emission peak of all samples was observed at around 370 nm. The noticed peak was significantly reduced in the case of the composites compared to pure B_4C and pure $AgFe_2O_4$. The photoluminescence emission initiates from the recombination rate of the photogenerated electron-hole pair. A decrease in the intensity of the emission peak indicates a lesser recombination possibility of the photoexcited carge carriers [26]. The significant reduction in the intensity of the emission peak belonging to the composite samples revealed that the photoexcited electron-hole pair could be separated vigorously at the composite interface. B_4C and $AgFe_2O_4$ was coupled in the composite matrix by ensuring the contact of the composite constituents to form a heterojunction structure, leading to the separation of the photoexcited charge carriers depending on the band energy differences of B_4C and $AgFe_2O_4$ [26]. The decrease in the recombination rate of the photogenerated charge carriers might positively affect the Cr(VI) photoreduction efficiency. Compared to $B_4C/AgFe_2O_4$(10/2), the $B_4C/AgFe_2O_4$(10/4) composite exhibited lower emission intensity (Fig. 3), which might provide advantages in terms of the Cr(VI) photoreduction efficiency.

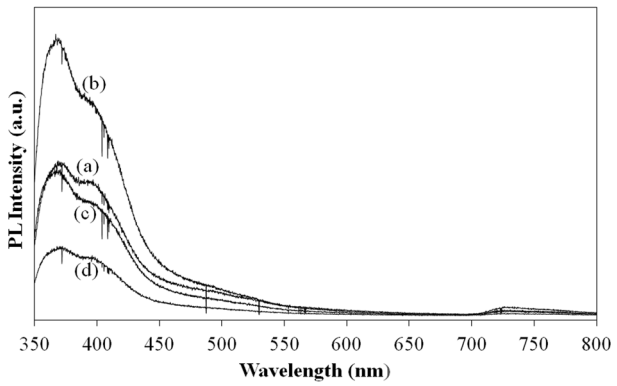

Fig. 3 Photoluminescence spectrum of **a** B_4C, **b** $AgFe_2O_4$, **c** $B_4C/AgFe_2O_4$(10/2) and **d** $B_4C/AgFe_2O_4$(10/4)

3.4 Surface area and pore volume characterization studies

The specific surface area and the porosity of B_4C, $AgFe_2O_4$ and $B_4C/AgFe_2O_4$(10/4) were investigated using N_2 adsorption-desorption studies. The N_2 adsorption-desorption isotherm of the as-prepared samples was characterized as Type IV according to the classification of isotherms proposed by IUPAC (Fig. 4) [53]. The surface area obtained by using Brunauer-Emmett-Teller (BET) method

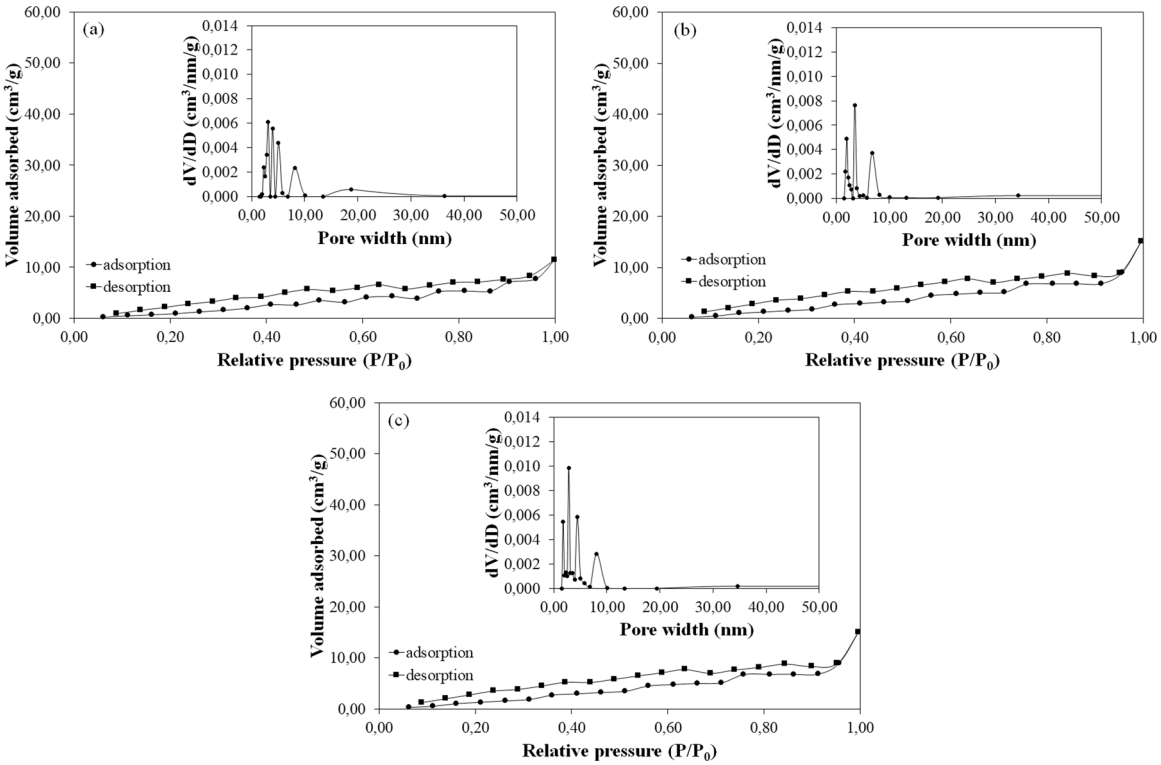

Fig. 4 N_2 adsorption-desorption isotherm (The insets exhibit the BJH pore size distribution) for **a** B_4C, **b** $AgFe_2O_4$, **c** $B_4C/AgFe_2O_4$(10/4)

were 10.6 m^2/g, 7.8 m^2/g and 8.3 m^2/g for B_4C, $AgFe_2O_4$ and $B_4C/AgFe_2O_4$(10/4), respectively. The pore size distribution of the samples was illustrated on the Barret-Joyner-Halender (BJH) plots (Fig. 4). According to the BJH plots, the average pore size was 3.1 nm, 3.5 nm and 2.8 nm for B_4C, $AgFe_2O_4$ and $B_4C/AgFe_2O_4$(10/4), respectively. In addition, the pore volume was found to be 0.023 cm^3/g, 0.041 cm^3/g, and 0.028 cm^3/g for B_4C, $AgFe_2O_4$, and $B_4C/AgFe_2O_4$(10/4), respectively. Compared to pure B_4C, there was a decrease in the average pore size and an increase in the pore volume of the composite sample. Materials with a pore size between 2–50 nm are known as mesoporous [54]. According to the results, all the samples had a mesoporous surface area. Since the Cr(VI) photoreduction reaction takes place on the photocatalyst surface, an enhanced surface area is important in terms of the photocatalytic reduction efficiency. The specific surface area of the prepared samples was close to each other. Hence, the effect of the surface area on the Cr(VI) photoreduction activity was not expected to be effective. On the other hand, the N_2 adsorption–desorption isotherm of the samples was comparable with a long first step between $P/P_0 = 0$-0.9 (Fig. 4), indicating partial narrowing of the opening of some pores during the synthesis of the photocatalyst samples [55].

3.5 Morphological analysis

FESEM images of B_4C exhibit irregular crystal structures varied between 1–5 µm (Fig. 5a). According to the FESEM images, B_4C crystal structures were successfully obtained. The presence of Ni catalyst and B_4C seed crystals might be the reason for the improved crystal structure obtained. On the other hand, $AgFe_2O_4$ crystals in the range of about 1–2 µm are illustrated on the FESEM images of $AgFe_2O_4$ (Fig. 5b). FESEM images of the composites exhibit crystal structures with a size of 1–10 µm (Fig. 5c, d). The recorded crystal structures might belong to both B_4C and $AgFe_2O_4$. The $B_4C/AgFe_2O_4$(10/2) composite had a similar microstructure with the $B_4C/AgFe_2O_4$(10/4) composite. No significant difference was observed on the FESEM images of both $B_4C/AgFe_2O_4$(10/2) and $B_4C/AgFe_2O_4$(10/4).

3.6 UV-Visible absorption study

Figure 6 illustrates UV-Vis absorption spectrum of the as-prepared samples. B_4C exhibited light absorption in the wavelength range of 200–230 nm, 230–560 nm, and 600–800 nm, respectively (Fig. 6a). The light absorption ability is important for the Cr(VI) photoreduction reaction. The incident light must be absorbed by the photocatalyst to form the photogenerated electron-hole pairs required for the Cr(VI) photoreduction reaction. According to the UV-Vis absorption spectrum, B_4C seemed to be suitable as a photocatalyst for the Cr(VI) photoreduction studies in the wavelength range of 200–800 nm. On the other hand, $AgFe_2O_4$ exhibited light absorption in the wavelength range of 200–220 nm, 220–270 nm, and 550-800 nm, respectively (Fig. 6b). The UV-Vis light absorption ability of B_4C and $AgFe_2O_4$ was similar to each other. All the composite samples exhibited high light absorption between 200–500 nm (Fig. 6c–g), implying that the $B_4C/AgFe_2O_4$ composites could be utilized both as UV light and visible-light-driven photocatalyst. Compared with pure B_4C and pure $AgFe_2O_4$, there was an increase in light absorption between 200–500 nm for the prepared composites, which indicated the successful coupling of B_4C with $AgFe_2O_4$. In parallel with the increase in the $AgFe_2O_4$ content of the composite, the intensity of the absorption band observed between 200–500 nm increased.

The Tauc Eq. (4) given below was employed to determine the optical band gap value of all samples [56]:

$$(\alpha h\nu)^2 = A\left(h\nu - E_g\right) \tag{4}$$

where α, hν, A, and E_g are the absorption coefficient, the photon energy of incoming light, a constant and the optical band gap value, respectively. The optical band gap value was determined by extrapolating the straight portion of $(\alpha h\nu)^2$ versus hν plots to the x-axis as shown in Fig. S1 [56]. The band gap value of pure B_4C and pure $AgFe_2O_4$ was found out to be 1.95 eV and 1.50 eV, respectively. In addition, the band gap value of $B_4C/AgFe_2O_4$(10/1), $B_4C/AgFe_2O_4$(10/2), $B_4C/AgFe_2O_4$(10/3), $B_4C/AgFe_2O_4$(10/4) and $B_4C/AgFe_2O_4$(10/5) was figured out to be 2.75 eV, 2.65 eV, 2.70 eV, 2.70 eV, and 2.75 eV, respectively. When compared with pure B_4C and pure $AgFe_2O_4$, there was an increase in the optical band gap value of the composites. Coupling B_4C with $AgFe_2O_4$ within the composite structure led to the optical band gap broadening, exhibiting a blue shift.

3.7 Photoreduction of Cr(VI) to Cr(III)

Figure S2 exhibits absorbance changes of Cr(VI)-diphenylcarbazide complex in the presence of pure B_4C, pure $AgFe_2O_4$, and the $B_4C/AgFe_2O_4$ composites. The absorbance of the Cr(VI)-diphenylcarbazide complex with the $B_4C/AgFe_2O_4$ composites was lower than that of pure B_4C and pure $AgFe_2O_4$. Figure 7 exhibits the photocatalytic reduction of Cr(VI) with time in the presence of the $B_4C/AgFe_2O_4$ composites. All the synthesized $B_4C/AgFe_2O_4$ composites exhibited enhanced photoreduction performance than that of the composite constituents. After 120 min. of visible light irradiation, the reduction rate of pure B_4C and pure $AgFe_2O_4$ was 65.1% and 21.7%, respectively. After 120 min. of visible light irradiation, 67.1%, 77.8%, 89.1%,

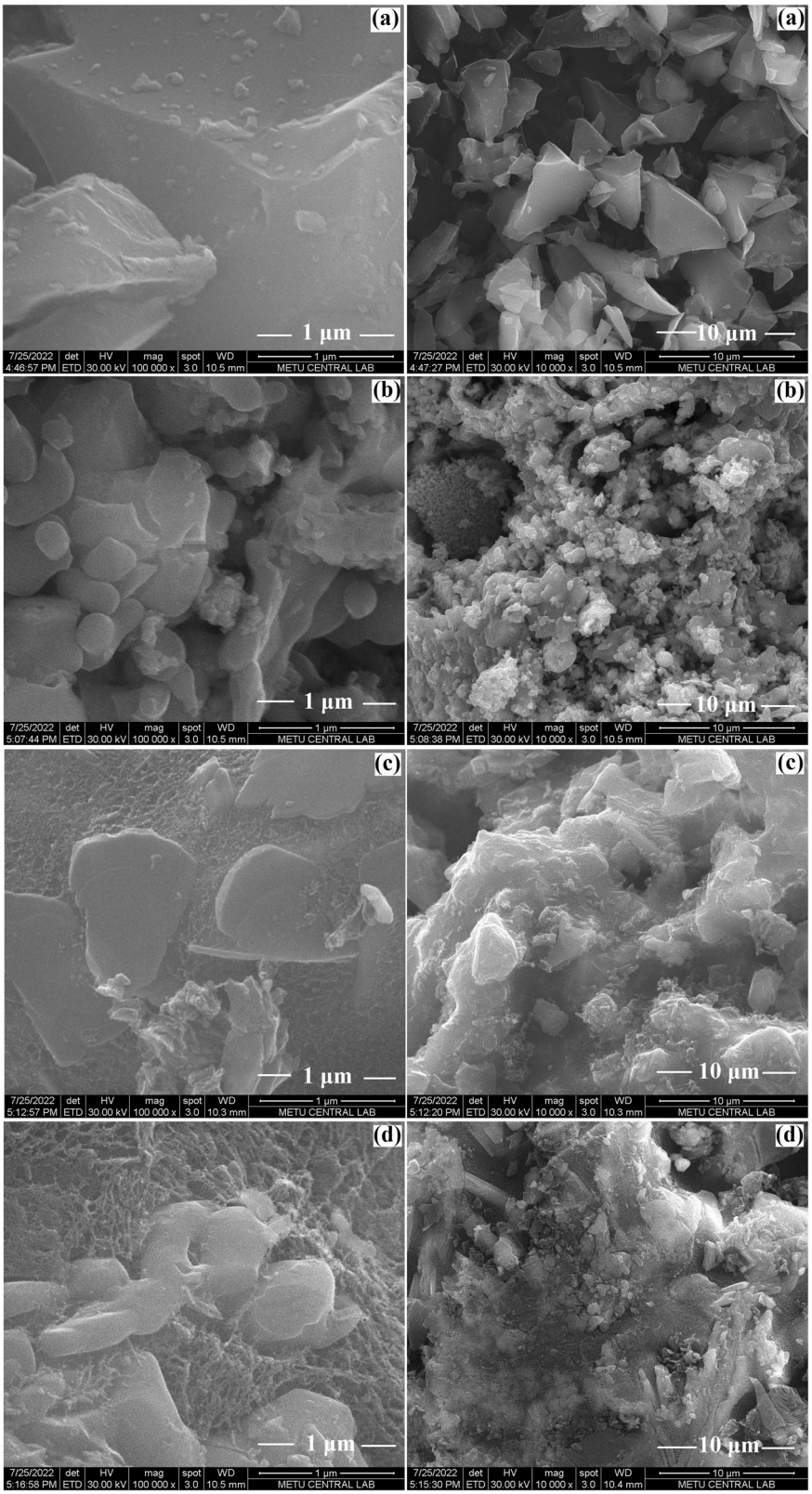

Fig. 5 FESEM images **a** B_4C, **b** $AgFe_2O_4$, **c** $B_4C/AgFe_2O_4(10/2)$ and **d** $B_4C/AgFe_2O_4(10/4)$

98.0% and 93.9% of the Cr(VI) was reduced by the $B_4C/AgFe_2O_4(10/1)$, $B_4C/AgFe_2O_4(10/2)$, $B_4C/AgFe_2O_4(10/3)$, $B_4C/AgFe_2O_4(10/4)$ and $B_4C/AgFe_2O_4(10/5)$ composite, respectively. The photoreduction performance of the $B_4C/AgFe_2O_4$ composites was improved with the increasing composition of $AgFe_2O_4$ in the composite and the

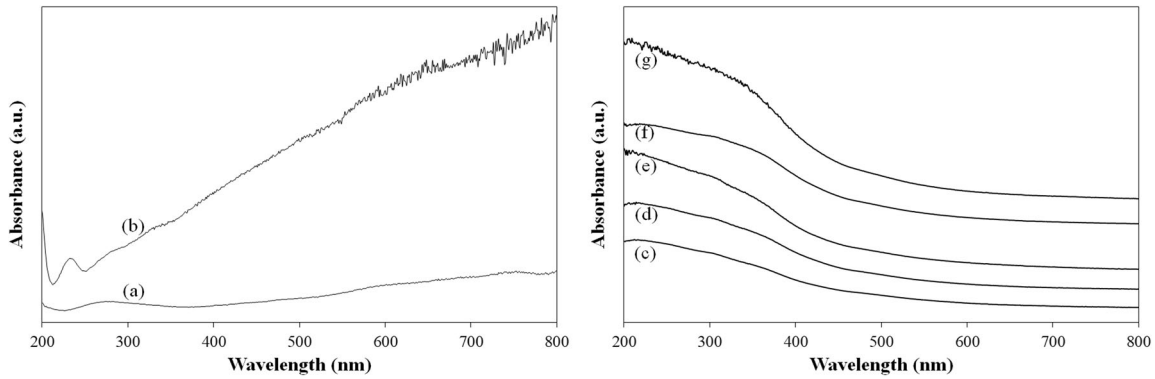

Fig. 6 UV-Vis absorption spectrum of **a** B_4C, **b** $AgFe_2O_4$, **c** $B_4C/AgFe_2O_4$(10/1), **d** $B_4C/AgFe_2O_4$(10/2), **e** $B_4C/AgFe_2O_4$(10/3), **f** $B_4C/AgFe_2O_4$(10/4) and **g** $B_4C/AgFe_2O_4$(10/5)

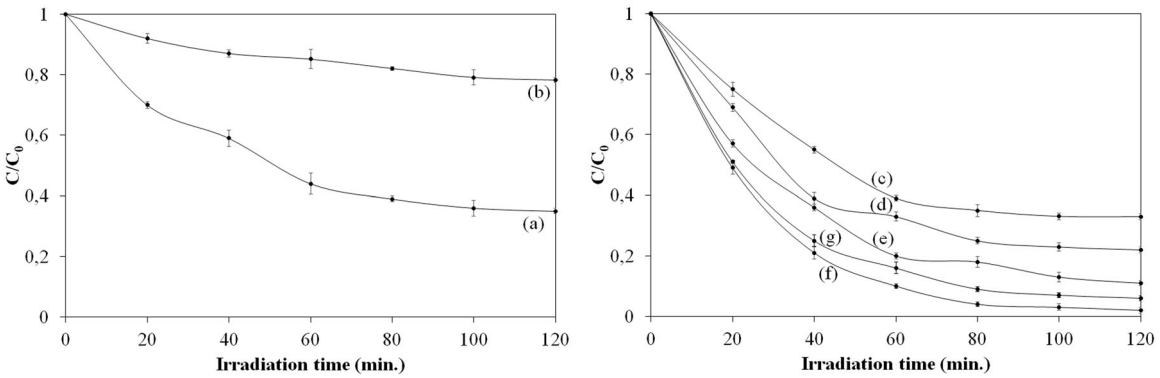

Fig. 7 Photoreduction rate of Cr(VI) in the presence of **a** B_4C, **b** $AgFe_2O_4$, **c** $B_4C/AgFe_2O_4$(10/1), **d** $B_4C/AgFe_2O_4$(10/2), **e** $B_4C/AgFe_2O_4$(10/3), **f** $B_4C/AgFe_2O_4$(10/4) and **g** $B_4C/AgFe_2O_4$(10/5)

optimized ratio of B_4C to $AgFe_2O_4$ was 10/4. The nano-sized ferrites and similar porous materials can exhibit high adsorption of pollutants due to their high surface area. The adsorption of Cr(VI) ions on the photocatalyst can contribute to the removal of Cr(VI) from an aqueous solution through the photoreduction technique [57, 58]. A control experiment was performed with pure B_4C, pure $AgFe_2O_4$, and $B_4C/AgFe_2O_4$(10/4) to check the effect surface adsorption alone. According to the results of the control experiment (Fig. S3), there was a negligible Cr(VI) photoreduction in the dark. The Cr(VI) removal rate in the presence of pure B_4C, pure $AgFe_2O_4$, and $B_4C/AgFe_2O_4$(10/4) were found out to be 10.4%, 11.2%, and 12.9%, respectively, within 120 min. This results revealed that the Cr(VI) removal rate by the adsorption process was very low compared to the removal rate by the photoreduction reaction. It was understood that the photoreduction reaction was dominant in the Cr(VI) removal process.

Figure 8 illustrates the proposed reaction mechanism of the Cr(VI) photoreduction under visible light irradiation. B_4C has a more positive conduction band potential than that of $AgFe_2O_4$ and they could form a heterojunction structure

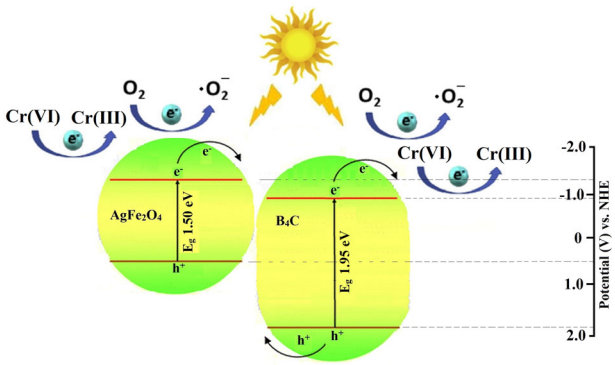

Fig. 8 Proposed photoreduction mechanism of Cr(VI) in the presence of the $B_4C/AgFe_2O_4$ composite

in the composite. Under visible light irradiation, electrons of both B_4C and $AgFe_2O_4$ are excited from the valence band to the conduction band. The photoexcited electrons of $AgFe_2O_4$ could transfer to the conduction band of B_4C and the photoinduced holes of B_4C could move to the valence band of $AgFe_2O_4$ due to the difference between the band potentials of B_4C and $AgFe_2O_4$ [25, 30, 59] (Fig. 8). In the

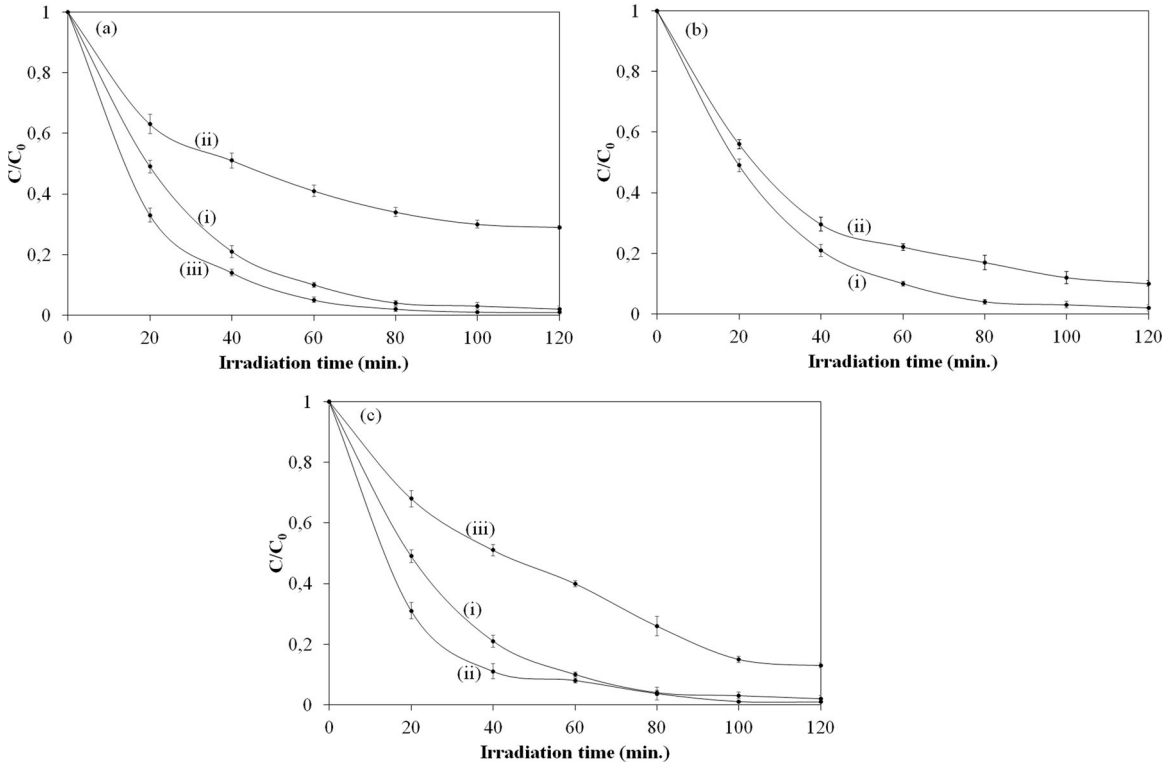

Fig. 9 **a** The Cr(VI) photoreduction efficiency of $B_4C/AgFe_2O_4$(10/4) (i) in the absence of a scavenger, (ii) in the presence of an electron scanvenger and (iii) in the presence of a hole scavenger; **b** The Cr(VI) photoreduction efficiency of $B_4C/AgFe_2O_4$(10/4) in the Cr(VI) solution prepared using (i) distilled water and (ii) real wastewater; **c** The Cr(VI) photoreduction efficiency of $B_4C/AgFe_2O_4$(10/4) (i) in the absence of an additive, (ii) in the presence of ammonium chloride and (iii) in the presence sodium sulfate

photoreduction process of Cr(VI) by the $B_4C/AgFe_2O_4$ composite under visible light irradiation, the photoexcited electrons in the conduction band of both B_4C and $AgFe_2O_4$ can transfer to the surface of the composite constituents, where Cr(VI) ions are reduced to Cr(III) ions with the following mechanisms [60]:

$$B_4C + hv \rightarrow e^- + h^+ \quad (5)$$

$$AgFe_2O_4 + hv \rightarrow e^- + h^+ \quad (6)$$

$$Cr_2O_7^{2-} + 14H^+ + 6e^- \rightarrow 2Cr^{3+} + 7H_2O \quad (7)$$

$$O_2 + e^- \rightarrow \cdot O_2^- \quad (8)$$

$$H_2O + h^+ \rightarrow \cdot OH + H^+ \quad (9)$$

The redox potential of the $Cr_2O_7{}^{-2}/Cr^{+3}$ couple (1.33 eV vs. NHE) is more positive than the conduction band position of B_4C and $AgFe_2O_4$ [25, 30, 60]. Both B_4C and $AgFe_2O_4$ can reduce the Cr(VI) ions using their photoexcited electrons. In addition, the redox potential of the O_2/O_2^- couple (−0.33 eV vs. NHE) is more positive than the conduction band potential of B_4C and $AgFe_2O_4$ [25, 30, 59]. Therefore, oxygen molecules can also be reduced by the photoinduced electrons of both semiconductors. On the other hand, the photogenerated holes can migrate to the surface of the semiconductors where they can oxidize H_2O molecules to hydroxyl (·OH) radicals. According the redox potential of the $H_2O/\cdot OH$ couple (2.27 eV vs. NHE), H_2O molecules could not be oxidized by the photogenerated holes of both B_4C and $AgFe_2O_4$ since the valence band potential of both semiconductors is more negative than the redox potential of the H_2O/OH couple [25, 30, 59].

3.8 Effect of scavengers, real wastewater, and additives on Cr (VI) photoreduction

The influence of electron and hole scavengers on the Cr(VI) photoreduction performance of the $B_4C/AgFe_2O_4$(10/4) composite was investigated (Fig. 9a). When potassium persulfate was added into the reaction medium, the Cr(VI) photoreduction efficiency was found to decrease from 98.0% to 77.1% at end of 120 min. of visible light irradiation (Fig. 9a). Potassium persulfate acted as an electron scavenger and might consume the photogenerated electrons in the conduction band of both semiconductors, leading to a reduction in the Cr(VI) photoreduction efficiency since some of the electrons required to reduce the Cr(VI) ions were consumed by the scavenger [40, 41]. When ammonium

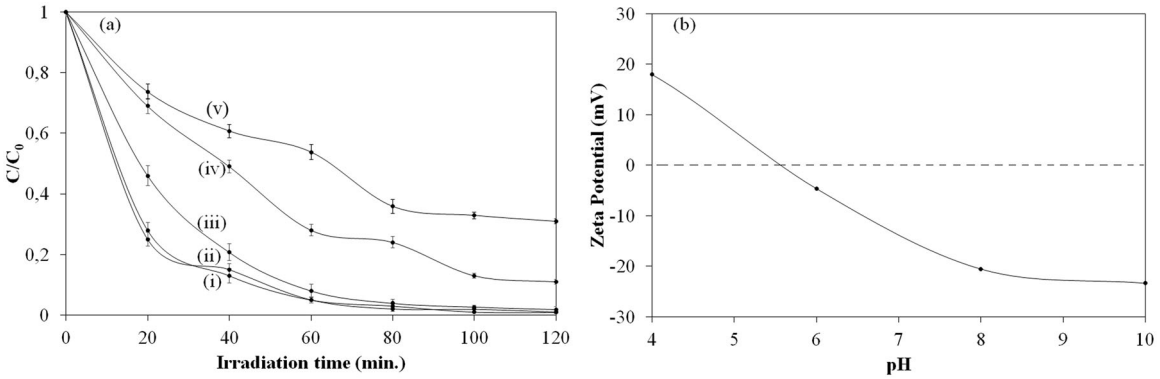

Fig. 10 **a** Effect of initial solution pH on the photoreduction rate of Cr(VI) in the presence of $B_4C/AgFe_2O_4$(10/4): (i) pH 2, (ii) pH 4, (iii) pH 6, (iv) pH 8 and (v) pH 10; **b** Zeta potential of $B_4C/AgFe_2O_4$(10/4) as a function of pH

oxalate was added into the Cr(VI) solution, the photoreduction efficiency of Cr(VI) increased from 98.0% to 99.1% within 120 min (Fig. 9a). This was because ammonium oxalate acted as a hole scavenger and it might consume the photogenerated holes in valence band of both semiconductors, leading to a suppression in the recombination of the photoexcited charge carriers and an enhancement in the photoreduction efficiency of Cr(VI) [41, 42].

In order to examine the effects of real wastewater environment on the photocatalytic removal of Cr(VI), the photoreduction of Cr(VI) experiment was also conducted in the real wastewater solution. When using real wastewater instead of distilled water to prepare the Cr(VI) solution, the Cr(VI) photoreduction efficiency of $B_4C/AgFe_2O_4$(10/4) decreased from 98.0% to 89.9% (Fig. 9b). Compared to the distilled water, there are different pollutants together with Cr(VI) ions in the real wastewater environment. There is a high probability of presence of coliform, pathogenic microorganisms, anions like SO_4^{2-}, NO^{3-}, NO^{2-}, Cl^- and PO_4^{3-}, and cations like Na^+, K^+, Li^+, and NH_4^+ in the real wastewater environment [45]. The specified pollutants might adhere to the surface of the $B_4C/AgFe_2O4$(10/4) composite, causing a narrowing of the surface area required for the Cr(VI) photoreduction reaction. The pollutants adsorbed on the surface of $B_4C/AgFe_2O_4$(10/4) might reduce the Cr(VI) photoreduction efficiency.

To understand the effect of the water matrix on the Cr(VI) photoreduction efficiency, ammonium chloride and sodium sulfate, commonly utilized in the wastewater treatment processes, were added into the Cr(VI) solution. The Cr(VI) photoreduction rate of $B_4C/AgFe_2O_4$(10/4) increased from 98.0% to 99.1% in the presence of ammonium chloride (Fig. 9c). Ammonium (NH_4^+) ion might act as a hole scavenger and improve the Cr(VI) photoreduction efficiency by reducing the recombination rate of the photogenerated charge carriers on $B_4C/AgFe_2O_4$(10/4) [45]. On the other hand, since sulfate ions can compete with Cr(VI) ions for adsorption at the active sites of $B_4C/AgFe_2O_4$(10/4), sulfate ion might inhibit the adsorption of Cr(VI) ions on the composite particles [61]. The competition of sulfate ions with Cr(VI) ions for adsorption might suppress the Cr(VI) photoreduction. The Cr(VI) photoreduction rate of $B_4C/AgFe_2O_4$(10/4) decreased from 98.0% to 87.1% in the presence of sodium sulfate (Fig. 9c). In addition, the photoreduced Cr(III) ions in the solution can be converted back to Cr(VI) ions through the oxidation reaction of Cr(III) with the sulfate ion [45], which might also be the reason for the reduction in the Cr(VI) removal rate in the presence of sodium sulfate.

3.9 Effect of pH and solution concentration on Cr(VI) photoreduction, reusability study

To evaluate the effect of the initial solution pH on the Cr(VI) photoreduction efficiency, Cr(VI) removal experiments were also conducted at pH 2, 4, 6, 8, and 10, respectively. The Cr(VI) removal performance of the $B_4C/AgFe_2O_4$(10/4) composite was evaluated by adsorption and photoreduction of Cr(VI). At pH 2, 4, and 6, the Cr(VI) removal rate of $B_4C/AgFe_2O_4$(10/4) was found out to be 99.1%, 98.9% vs 98.2%, respectively, within 120 min. (Fig. 10a). Compared to the Cr(VI) removal rate obtained with the $B_4C/AgFe_2O_4$(10/4) composite in the neutral solution (Fig. 7), there was a slight increase in the Cr(VI) removal rate in acidic solutions. At pH 8 and 10, the Cr(VI) photoreduction efficiency was 88.8% and 69.2%, respectively, at the end of 120 min. of visible light irradiation (Fig. 10a). When compared with the Cr(VI) reduction rate obtained with $B_4C/AgFe_2O_4$(10/4) in the neutral solution (Fig. 7), there was a significant reduction in the Cr(VI) reduction rate in basic solutions. At lower pH conditions (pH < 7), there might be two main Cr(VI) ions, $Cr_2O_7^{2}$ and $HCrO^{4-}$, which could be easily reduced to Cr(III) ions through the

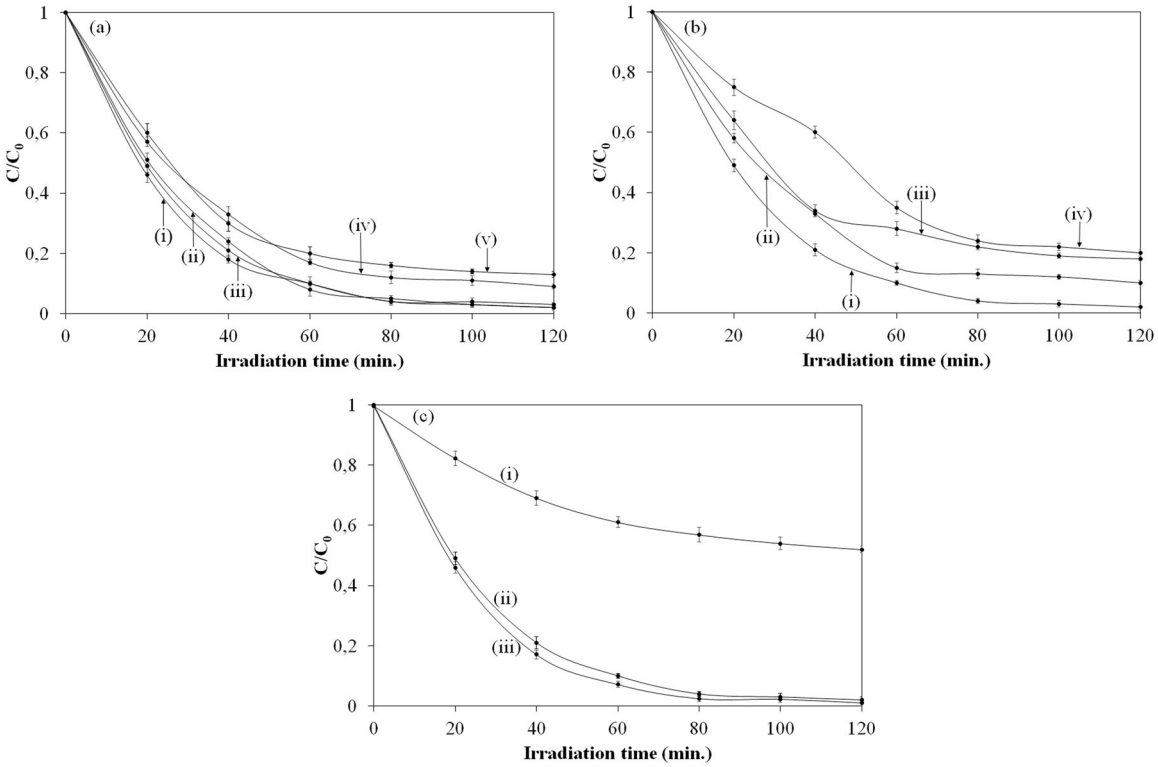

Fig. 11 **a** The Cr(VI) photoreduction efficiency of $B_4C/AgFe_2O_4$(10/4) with different initial solution concentration of Cr(VI): (i) 10 mg/l, (ii) 15 mg/l, (iii) 20 mg/l, (iv) 25 mg/l and (v) 30 mg/l; **b** The reusability results of the Cr(VI) photoreduction experiment in the presence of $B_4C/AgFe_2O_4$(10/4): (i) first cycle, (ii) second cycle, (iii) third cycle and (iv) fourth cycle; **c** Effect of the $B_4C/AgFe_2O_4$(10/4) concentration ((i) 0.1 g/l, (ii) 0.5 g/l and (iii) 1 g/l) on the Cr(VI) photoreduction efficiency

following reactions [62, 63]:

$$14H^+ + Cr_2O_7^{2-} + 6e^- \rightarrow 2Cr^{3+} + 7H_2O \quad (10)$$

$$7H^+ + HCrO^{4-} + 3e^- \rightarrow Cr^{3+} + 4H_2O \quad (11)$$

At higher pH conditions (pH > 7), CrO_4^{2-} might be the dominate ion in the reaction medium. CrO_4^{2-} ions could be reduced to Cr(III) ions according to the following reaction [62, 63]:

$$CrO_4^{2-} + 4H_2O + 3e^- \rightarrow Cr(OH)_3(s) + 5OH^- \quad (12)$$

The decrease in the Cr(VI) photoreduction efficiency at pH 8 and 10 might be due the formation $Cr(OH)_3$ precipication, blocking the active sites of the photocatalyst required for the Cr(VI) removal [62, 63]. Under acidic conditions, the dominant species in the Cr(VI) solution, $Cr_2O_7^{2-}$ and $HCrO^{4-}$, have negative charges. According to Fig. 10b, when the pH of the initial solution was adjusted to 2 and 4, the pH of the initial solution was below the point of zero charge (PZC) of the $B_4C/AgFe_2O_4$(10/4) composite. Because of the positively charged of the surface of $B_4C/AgFe_2O_4$ at pH 4 and below (Fig. 10b), more Cr(VI) ions might be adsorbed on the surface of the composite photocatalyst with a strong electrostatic interaction, promoting the Cr(VI) photoreduction [45, 64]. When the pH of the initial solution was above 7, the pH of the initial solution was above the PZC value of the $B_4C/AgFe_2O_4$(10/4) composite (Fig. 10b). Under basic conditions, the dominant Cr(VI) ions, CrO_4^{2-} species, might have less tendency to be adsorbed on the surface the $B_4C/AgFe_2O_4$ composite, suppressing the Cr(VI) photoreduction. The removal rate of Cr(VI) reached to almost 99% at pH 2 and 4 due to the positive synergistic effect of adsorption and photoreduction processes of Cr(VI) ions [45, 64].

The effect of the initial solution concentration on the Cr(VI) removal performance is important for practical application [23]. Different initial solution concentrations of Cr(VI) (10, 15, 20, 25, and 30 mg/l) were studied and their results are shown in Fig. 11a. The Cr(VI) photoreduction rate of $B_4C/AgFe_2O_4$(10/4) at the intitial solution concentration of 10, 15, 20, 25 and 30 mg/l were 96.8%, 97.8%, 98.0%, 90.9%, and 86.9%, respectively, within 120 min (Fig. 11a). The Cr(VI) removal rates obtained with the initial solution concentration of 10 mg/l, 15 mg/l, and 20 mg/l were close to each other. A small decrease was observed in the Cr(VI) photoreduction rate obtained with the initial solution concentration of 25 mg/l and 30 mg/l. For

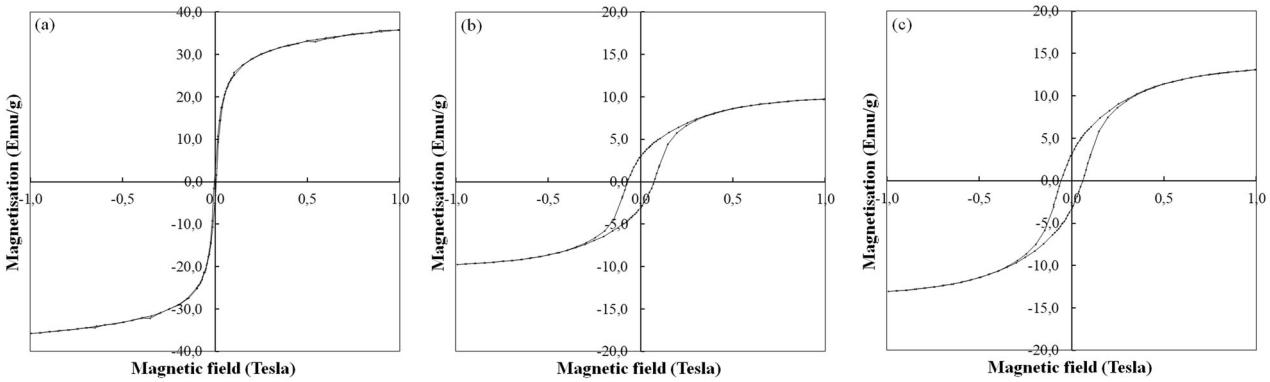

Fig. 12 Magnetic hysteresis loop of **a** $AgFe_2O_4$, **b** $B_4C/AgFe_2O_4(10/2)$ and **c** $B_4C/AgFe_2O_4(10/4)$

a fixed amount of the photocatalyst, the total available surface area and the photogenerated charge carriers were limited to enhance the Cr(VI) photoreduction efficiency at a higher solution concentration [23, 64]. In addition, there might be a decrease in the light transmittance of the Cr(VI) solution in parallel with the increase in the initial solution concentration, leading to a decrease in the amount of the incident light absorbed by the photocatalyst. The specified facts might be the reason for the observed decrease in the Cr(VI) photoreduction efficiency at the initial solution concentration of 25 mg/l and 30 mg/l.

The reusability of the photocatalyst is also important from application point of view. At the end of each photoreduction cycle, the $B_4C/AgFe_2O_4(10/4)$ composite particles were removed from the Cr(VI) solution by magnetic separation and cleaned. Then, they were utilized in the following photoreduction cycle. The Cr(VI) removal rate in the presence of the $B_4C/AgFe_2O_4(10/4)$ composite reduced from 98.0% to 79.9% at the fourth photoreduction cycle (Fig. 11b), which indicated that the $B_4C/AgFe_2O_4(10/4)$ composite exhibited relativelty good reusability. FTIR spectrum, XRD diffractogram and FESEM images of untreated $B_4C/AgFe_2O_4(10/4)$ and four times of recycled $B_4C/AgFe_2O_4(10/4)$ were similar to each other (Figs. S4 and S5). There were no additional peaks on the FTIR spectrum and the XRD diffractogram of four times of recycled $B_4C/AgFe_2O_4(10/4)$. In addition, there was no significant change in the position and the intensity of the present peaks (Fig. S4). According to the FESEM images, both the untreated sample and the four times of recycled sample have similar morphology (Fig. S5). Similar peaks belonging to B, C, Ag, Fe, and O elements are seen on the EDX spectrum (Fig. S5). The indicated analyses confirmed that the four times of recycled $B_4C/AgFe_2O_4(10/4)$ retained its structure and surface morphology after 480 min. of visible light irradiation. Some semiconductor photocatalysts such as TiO_2 [65] and ZnO [66] can decompose the carbon bonds during the photocatalytic reactions depending on the intensity of the light source and the irradiation time. The photocatalytic decomposition effect of $AgFe_2O_4$ on B_4C was also checked by the EDX spectroscopy. However, there was no significant difference in the peak intensity of C element on the EDX spectrum of both untreated $B_4C/AgFe_2O_4(10/4)$ and four times of recycled $B_4C/AgFe_2O_4(10/4)$. Limiting the irradiation time to 2 h might also have an effect on this result [65, 66]. Uncontrolled release of Ag ions from the photocatalyst into the aqueous solution is not only wasteful but also important in terms of the EPA recommended limit of silver ions (0.1 ppm) [67, 68]. According to the EDX spectrum of both the untreated $B_4C/AgFe_2O_4(10/4)$ and the four times of recycled $B_4C/AgFe_2O_4(10/4)$, there was no significant change in the peak intensity of the Ag element, meaning that the uncontrolled release of Ag ions might be at low level. In addition, the mesoporous surface structure of the $B_4C/AgFe_2O_4(10/4)$ composite can prevent the Ag ions from being released into the aqueous solution [67, 68].

The effect of the photocatalyst concentration on the Cr(VI) removal rate was also investigated by varying the $B_4C/AgFe_2O_4(10/4)$ composition in the range of 0.1–1.0 g/l. The Cr(VI) removal rate enhanced with increasing the photocatalyst concentration and it decreased with decreasing the $B_4C/AgFe_2O_4(10/4)$ concentration. When the $B_4C/AgFe_2O_4(10/4)$ concentration in the Cr(VI) solution was changed from 0.5 g/l to 0.1 g/l and 1.0 g/l, the Cr(VI) removal rate was observed to be 48.1% and 98.9%, respectively (Fig. 11c). The noticed change in the Cr(VI) removal rate was assigned to the availability of active sites on the photocatalyst for the photoreduction reaction. If there was a decrease in the quantity of the photocatalyst, the number of active sites also decreased, leading to the reduction in the Cr(VI) photoreduction efficiency [69].

3.10 Magnetic property

The magnetic hysteresis loop of the as-prepared samples is exhibited in Fig. 12. The saturation magnetization values are 35.8 emu/g, 9.8 emu/g ve 13.1 emu/g for $AgFe_2O_4$, $B_4C/$

$AgFe_2O_4$(10/2) and $B_4C/AgFe_2O_4$(10/4), respectively. The relatively high value of the saturation magnetization obtained by pure $AgFe_2O_4$ might be due to the higher degree of crystallinity with a small amount of inert surface layers [70]. In addition, the heat treatment process applied following the $AgFe_2O_4$ synthesis might rearrange the distribution of the silver and iron ions in the octahedral and tetrahedral sites, which might also be the reason for the relatively high value of the saturation magnetization [70]. The $B_4C/AgFe_2O_4$(10/4) composite with a higher $AgFe_2O_4$ composition provided higher saturation magnetization value when compared with the $B_4C/AgFe_2O_4$(10/2) composite. According to these results, $AgFe_2O_4$, $B_4C/AgFe_2O_4$(10/2), and $B_4C/AgFe_2O_4$(10/4) can be easily recycled from the wastewater environment by magnetic separation [71].

4 Conclusion

The $B_4C/AgFe_2O_4$ composites were investigated as a visible light-driven photocatalyst for the Cr(VI) photoreduction. All of the composites with five different $B_4C/AgFe_2O_4$ ratio were found to be effective for the Cr(VI) removal photoreduction, but the highest removal rate was obtained by the $B_4C/AgFe_2O_4$ ratio of 10/4. Coupling B_4C with $AgFe_2O_4$ enhanced the Cr(VI) photoreduction efficiency by promoting separation of the photogenerated electron-hole pairs between the composite interface. The photogenerated electrons on the conduction band of both B_4C and $AgFe_2O_4$ might convert highly toxic Cr(VI) to less toxic Cr(III) ions. The real wastewater environment affected the Cr(VI) photoreduction efficiency. The removal rate decreased from 98.0% to 89.9% within 120 min. of visible light irradiation. In addition, the additives in the water matrix, the initial solution concentration, the photocatalyst concentration and the initial solution pH had pronounced effect on the Cr(VI) photoreduction efficiency. While the Cr(VI) removal rate increased under acidic conditions, the removal value significantly decreased under basic conditions. According to the reusability experiments, the Cr(VI) removal rate decreased from 98.0% to 79.9% at the fourth photoreduction cycle.

Author contributions All authors contributed to the study's conception and design. Material preparation, data collection, and analysis were performed by OK and HNK.

Funding This research has been supported by The Scientific and Technological Research Council of Turkey (TÜBİTAK) with the Project Number 120M005.

Compliance with ethical standards

Conflict of interest The authors declare no competing interests.

References

1. Wang XS, Chen CH, Ichihara F, Oshikiri M, Liang J, Li L, Li YX, Song H, Wang SY, Zhang T (2019) Integration of adsorption and photosensitivity capabilities into a cationic multivariate metal-organic framework for enhanced visible-light photoreduction reaction. Appl Catal B-Environ 253:323–330
2. Anthony ET, Oladoja NA (2022) Process enhancing strategies for the reduction of Cr(VI) to Cr(III) via photocatalytic pathway. Environ Sci Pollut Res 29:8026–8053
3. He C, Zhang B, Jiang Y, Liu H, Zhao HP (2021) Microbial electrolysis cell produced biogas as sustainable electron donor for microbial chromate reduction. Chem Eng J 403:126429
4. Jadhav SA, Garud HB, Thoravat SS, Patil VS, Shinde PS, Burungale SH, Patil PS (2021) Synthesis and testing of functional mesoporous silica nanoparticles for removal of Cr(VI) ions from water. Biointerface Res Appl Chem 11(2):8599–8607
5. Ou JH, Sheu YT, Tsang DCW, Sun YJ, Kao CM (2020) Application of iron/aluminum bimetallic nanoparticle system for chromium-contaminated groundwater remediation. Chemosphere 256:127158
6. Roy S, Majumdar S, Sahoo GC, Bhowmick S, Kundu AK, Mondal P (2020) Removal of As(V), Cr(VI) and Cu(II) using novel amine functionalized composite nanofiltration membranes fabricated on ceramic tubular substrate. J Hazard Mater 399:122841
7. Sun J, Cao FM, Zhang L, Sun YQ (2022) The low-cost and high-efficient photoreduction of Cr(VI) by oxalic acid synergized with the iron-loaded rice straw. J Mol Liq 351:118552
8. Guo ZP, Wei W, Li YH, Li ZY, Hou FM, Wei A (2022) Cr(VI)-imprinted polymer wrapped on urchin-like Bi2S3 for reduced photocorrosion and improved photoreduction of aqueous Cr(VI). J Hazard Mater 422:126946
9. Canterino M, Di Somma I, Marotta R, Andreozzi R (2008) Kinetic investigation of Cu(II) ions photoreduction in presence of titanium dioxide and formic acid. Water Res 42:4498–4506
10. Coelho FEB, Candelario VM, Rodrigues AEM, Santos MTL, Magnacca G (2020) Photocatalytic reduction of Cr(VI) in the presence of humic acid using immobilized Ce-ZrO_2 under visible light. Nanomaterials 10(4):779
11. Xu Z, Xu J, Ni J, Hu F, Xu J (2019) Visible light catalytic reduction of Cr(VI) by palygorskite modified with CuO in the presence of tartaric acid. Environ Eng Sci 36(4):491–498
12. Hu D, Song C, Jin X, Huang Q (2020) Polymer solution-assisted assembly of hierarchically nanostructured ZnO onto 2D neat graphene sheets with excellent photocatalytic performance. J Alloy Compd 843:156030
13. Wang M, Zeng Y, Dong G, Wang C (2020) Br-doping of g-C3N4 towards enhanced photocatalytic performance in Cr(VI) reduction. Chin J Catal 41(10):1498–1510
14. Yan DJ, Liu JK, Fu XC, Liu PL, Luo HA (2019) Low-temperature synthesis of mesoporous boron carbides as metal-free photocatalysts for enhanced CO_2 reduction and generation of hydroxyl radicals. J Mater Sci 54:6151–6163
15. Yanase I, Ogaware R, Kobayashi H (2009) Synthesis of boron carbide powder from polyvinyl borate precursor. Mater Lett 63:91–93
16. Kesici AD, Kiraz N (2021) Low-temperature synthesis of boron carbide nanofibers via electrospinning to reinforce composites. Chem Pap 75:5839–5848
17. Mondal S, Banthia AK (2005) Low-temperature synthetic route for boron carbide. J Eur Ceram Soc 25:287–291
18. Ding DH, Bai B, Xiao GQ, Luo JY, Chong XC (2021) Molten-salt-assisted combustion synthesis of B4C powders: Synthesis mechanism and dielectric and electromagnetic wave absorbing properties. Ceram Int 47(13):18708–18719

19. Zhang S, Lu WZ, Wang CB, Shen Q, Zhang LM (2012) Synthesis and characterization of $B_{13}C_2$ boron carbide ceramic by pulsed electric current. Ceram Int 38:895–900
20. Volger KW, Kroke E, Gervais C, Saito T, Babonneau F, Riedel R, Iwamoto Y, Hirayama T (2003) B/C/N materials and B4C synthesized by a non-oxide sol-gel process. Chem Mater 15:755–764
21. Sun Y, Chintersingh KL, Schoenitz M, Dreizin EL (2019) Reactive shell model for boron oxidation. J Phys Chem C 123(18):11807–11813
22. da Rocha RM, de Melo FCL (2010) Synthesis of fine B4C powder using B4C seeding in carbothermal reduction process. Mater Sci Forum 660-661:948–953
23. Liu JK, Wen SH, Hou Y, Zuo F, Beran GJO, Feng PY (2013) Boron carbides as efficient, metal-free, visible-light-responsive photocatalysts. Angew Chem Int Ed 52:3241–3245
24. Zhang XJ, Wang L, Du QC, Wang ZY, Ma SG, Yu M (2016) Photocatalytic CO_2 reduction over B_4C/C_3N_4 with internal electric field under visible light irradiation. J Colloid Interface Sci 464:89–95
25. Lv YF, Liu Y, Wei J, Li MY, Xu DY, Lai B (2021) Bisphenol S degradation by visible light assisted peroxymonosulfate process based on BiOI/B4C photocatalysts with Z-scheme heterojunction. Chem Eng J 417:129188
26. Zhang XJ, Yang JP, Cai TC, Zuo GQ, Tang CQ (2018) TiO_2 nanosheets decorated with B4C nanoparticles as photocatalysts for solar fuel production under visible light irradiation. Appl Surf Sci 443:558–566
27. Koysuren O, Koysuren HN (2022) Preparation and activity evaluation of B_4C/ZnO composite photocatalyst. J Sol-Gel Sci Technol 103(1):172–184
28. Mao Y, Qiu JP, Zhang PQ, Fei ZX, Bian CQ, Janani BJ, Fakhri A (2022) A strategy of silver Ferrite/Bismuth ferrite nano-hybrids synthesis for synergetic white-light photocatalysis, antibacterial systems and peroxidase-like activity. J Photochem Photobio A-Chem 426:113756
29. Singh H, Rajput JK, Dogra N, Jain G, Gupta A, Garg S (2021) A novel sucrose chelated visible-light sensitive AFO NPs: preparation, characterization, photocatalytic activity, and reaction mechanism. J Aust Ceram Soc 57(3):835–848
30. Nas MS (2021) $AgFe_2O_4$/MWCNT nanoparticles as novel catalyst combined adsorption-sonocatalytic for the degradation of methylene blue under ultrasonic irradiation. J Environ Chem Eng 9(3):105207
31. Rekhila G, Trari M, Bessekhouad Y (2017) Characterization and application of the hetero-junction $ZnFe_2O_4/TiO_2$ for Cr(VI) reduction under visible light. Appl Water Sci 7(3):1273–1281
32. Anthony ET, Lawal IA, Bankole MO, Klink M, Ololade IA, Oladoja NA (2020) Solar active heterojunction of p-$CaFe_2O_4$/n-ZnO for photoredox reactions. Environ Technol Innov 20:101060
33. Nasrallah N, Kebir M, Koudri Z, Trari M (2011) Photocatalytic reduction of Cr(VI) on the novel hetero-system $CuFe_2O_4$/CdS. J Hazard Mater 185(2-3):1398–1404
34. Sin JC, Lam SM, Zeng HH, Lin H, Li HX, Tham KO, Mohamed AR, Lim JW, Qin ZZ (2021) Magnetic $NiFe_2O_4$ nanoparticles decorated on N-doped BiOBr nanosheets for expeditious visible light photocatalytic phenol degradation and hexavalent chromium reduction via a Z-scheme heterojunction mechanism. Appl Surf Sci 559:149966
35. Jiang ZK, Chen KX, Zhang YC, Wang YY, Wang F, Zhang GS, Dionysiou DD (2020) Magnetically recoverable $MgFe_2O_4$/conjugated polyvinyl chloride derivative nanocomposite with higher visible-light photocatalytic activity for treating Cr(VI)-polluted water. Sep Purif Technol 236:11627
36. Sanadi KR, Kamble GS (2018) Novel synthesis of silver ferrite by sol-gel auto combustion method and study of its photocatalytic activity. Adv Porous Mater 6(1):41–44
37. Shen Y, Li XY, Zhao QD, Hou Y, Tade M, Liu SM (2011) Facile synthesis and characterization of $ZnFe_2O_4$/alpha-Fe_2O_3 composite hollow nanospheres. Mater Res Bull 46(12):2235–2239
38. Lace A, Ryan D, Bowkett M, Cleary J (2019) Chromium monitoring in water by colorimetry using optimised 1,5-Diphenylcarbazide Method. Int J Environ Res Public Health 16(10):1803
39. Oladoja NA, Anthony ET, Ololade IA, Saliu TD, Bello GA (2018) Self-propagation combustion method for the synthesis of solar active Nano Ferrite for Cr(VI) reduction in aqua system. J Photochem Photobiol A-Chem 353:229–239
40. Li X, Chen D, Li N, Xu Q, Li H, He J, Lu J (2020) Efficient reduction of Cr(VI) by a BMO/Bi_2S_3 heterojunction via synergistic adsorption and photocatalysis under visible light. J Hazard Mater 400:123243
41. Hasija V, Raizada P, Singh P, Verma N, Khan AAP, Singh A, Selvasembian R, Kim SY, Hussain CM, Nguyen VH (2021) Progress on the photocatalytic reduction of hexavalent Cr (VI) using engineered graphitic carbon nitride. Process Saf Environ Prot 152:663–678
42. Challagulla S, Nagarjuna R, Ganesan R, Roy S (2016) Acrylate-based polymerizable sol-gel synthesis of magnetically recoverable TiO_2 supported Fe_3O_4 for Cr(VI) photoreduction in aerobic atmosphere. ACS Sustain Chem Eng 4:974–982
43. Wu Y, Chen C, He S, Zhao X, Huang S, Zeng G, You Y, Cao Y, Niu L (2021) In situ preparation of visible-light-driven carbon quantum dots/$NaBiO_3$ hybrid materials for the photoreduction of Cr(VI). J Environ Sci 99:100–109
44. Assadi A, Dehghani MH, Rastkari N, Nasseri S, Mahvi AH (2012) Photocatalytic reduction of hexavalent chromium in aqueous solution with zinc oxide nanoparticles and hydrogen peroxide. Environ Prot Eng 38(4):5–16
45. Cheng Q, Wang C, Doudrick K, Chan CK (2015) Hexavalent chromium removal using metal oxide photocatalysts. Appl Catal B-Environ 176:740–748
46. SarithaDevi HV, Swapna MS, Sankararaman S (2021) Boron carbide nanowires from castor oil for optronic applications: a low-temperature greener approach. J Mater Sci: Mater Electron 32:7391–7398
47. Park J, Her S, Cho S, Woo SM, Bae S (2022) Synthesis and characterization of Polyethylene/B4C composite, and its neutron shielding performance in cementitious materials: Experimental and simulation studies. Cem Concr Compos 129:104458
48. Chen XW, Dong SM, Kan YM, Zhou HJ, Hu JB, Ding YS (2016) Effect of glycerine addition on the synthesis of boron carbide from condensed boric acid-polyvinyl alcohol precursor. RSC Adv 6(11):9338–9343
49. SarithaDevi HV, Swapna MS, Ambadas G, Sankararaman S (2018) Low-temperature green synthesis of boron carbide using aloe vera. Chin Phys B 27(10):107702
50. Kakiage M, Tahara N, Yanagidani S, Yanase I, Kobayashi H (2011) Effect of boron oxide/carbon arrangement of precursor derived from condensed polymer-boric acid product on low-temperature synthesis of boron carbide powder. J Ceram Soc Jpn 119:422–425
51. ElNahrawy AM, Mansour AM, ElAttar HA, Sakr EMM, Soliman AA, Abou Hammad AB (2020) Impact of Mn-substitution on structural, optical, and magnetic properties evolution of sodium-cobalt ferrite for opto-magnetic applications. J Mater Sci Mater Electron 31(8):6224–6232
52. Jasrotia D, Singh B, Kumar A, Verma SK, Alvi PA, Kumar K, Sridhar B (2019) $[HgCl_4](2-)[C_5H_6N_2Cl](2+)$ inorganic-organic hybrid material with structural and optical properties. Results Phys 14:102421
53. Rebekah A, Anantharaj S, Viswanthan C, Ponpandian N (2020) Zn-substituted $MnCo_2O_4$ nanostructure anchored over rGO for

boosting the electrocatalytic performance towards methanol oxidation and oxygen evolution reaction (OER). Int J Hydrog Energy 45(29):14713–14727
54. Ugraskan V, Isik B, Yazici O (2022) Adsorptive removal of methylene blue from aqueous solutions by porous boron carbide: isotherm, kinetic and thermodynamic studies. Chem Eng Commun 209(8):1111–1129
55. Salameh C, Nogier JP, Launay F, Boutros M (2015) Dispersion of colloidal TiO_2 nanoparticles on mesoporous materials targeting photocatalysis applications. Catal Today 257:35–40
56. Qiu YF, Fan HB, Tan GP, Yang ML, Yang XX, Yang SH (2014) Effect of nitrogen doping on the photo-catalytic properties of nitrogen-doped ZnO tetrapods. Mater Lett 131:64–66
57. Meidanchi A, Akhavan O (2014) Superparamagnetic zinc ferrite spinel-graphene nanostructures for fast wastewater purification. Carbon 69:230–238
58. Wang LX, Li JC, Wang YQ, Zhao LJ, Jiang Q (2012) Adsorption capability for Congo red on nanocrystalline MFe_2O_4 (M = Mn, Fe, Co, Ni) spinel ferrites. Chem Eng J 181:72–79
59. Villa K, Galan-Mascaros JR (2021) Nanostructured photocatalysts for the production of methanol from methane and water. Chemsuschem 14:2023–2033
60. Palve AM (2021) Ultra-fast photoreduction of toxic Cr(VI) by CdS-rGO synthesized using single source precursor. J Alloy Compd 868:159143
61. Hu XJ, Wang WX, Xie GY, Wang H, Tan XF, Jin Q, Zhou DX, Zhao YL (2019) Ternary assembly of g-C3N4/graphene oxide sheets /$BiFeO_3$ heterojunction with enhanced photoreduction of Cr(VI) under visible-light irradiation. Chemosphere 216:733–741
62. Jia LX, Tan X, Li YF, Zhang YZ, Cao SQ, Zhou W, Huang X, Liu LQ, Yu T (2022) Design of $BiOBr_{0.25}I_{0.75}$ for synergy photoreduction Cr(VI) and capture Cr(III) over wide pH range. Chin Chem Lett 33(6):3053–3060
63. Wang D, Xu Y, Jing L, Xie M, Song Y, Xu H, Li H, Xie J (2020) In situ construction efficient visible-light-driven three-dimensional Polypyrrole/$Zn3In_2S6$ nanoflower to systematically explore the photoreduction of Cr(VI): Performance, factors and mechanism. J Hazard Mater 384:121480
64. Izzudin NM, Jalil AA, Aziz FFA, Azami MS, Ali MW, Hassan NS, Rahman AFA, Fauzi AA, Vo DVN (2021) Simultaneous remediation of hexavalent chromium and organic pollutants in wastewater using period 4 transition metal oxide-based photocatalysts: a review. Environ Chem Lett 19(6):4489–4517
65. Akhavan O, Abdolahad M, Esfandiar A, Mohatashamifar M (2010) Photodegradation of graphene oxide sheets by TiO_2 nanoparticles after a Photocatalytic Reduction. J Phys Chem C 114(30):12955–12959
66. Akhavan O (2010) Graphene nanomesh by ZnO nanorod photocatalysts. ACS Nano 4(7):4174–4180
67. Furlan PY, Furlan AY, Kisslinger K, Melcer ME (2021) Templated mesoporous silica outer shell for controlled silver release of a magnetically recoverable and reusable nanocomposite for water disinfection. ACS Appl Mater Interfaces 13(40):47972–47986
68. Akhavan O, Ghaderi E (2010) Self-accumulated Ag nanoparticles on mesoporous TiO_2 thin film with high bactericidal activities. Surf Coat Technol 204(21-22):3676–3683
69. Tambat S, Umale S, Sontakke S (2016) Photocatalytic degradation of Milling Yellow dye using sol-gel synthesized CeO_2. Mater Res Bull 76:466–472
70. Chia CH, Zakaria S, Yusoff M, Goh SC, Haw CY, Ahmadi S, Huang NM, Lim HN (2010) Size and crystallinity-dependent magnetic properties of $CoFe_2O_4$ nanocrystals. Ceram Int 36(2):605–609
71. Zhang EL, Wang LJ, Zhang BG, Xie YP, Wang GS (2019) Shape-controlled hydrothermal synthesis of $CuFe_2O_4$ nanocrystals for enhancing photocatalytic and photoelectrochemical performance. Mater Chem Phys 235:121633